



Construction of a programmed activation nanosystem based on intracellular hypoxia in cisplatin-resistant tumor cells for reversing cisplatin resistance

Yurong Liu^{a,1}, Longqing Si^{a,1}, Yunheng Liu^{a,1}, Song Li^a, Xiaokang Zhang^a, Shaojing Jiang^b, Wenjing Liu^a, Xiaolin Li^a, Lianguo Zhang^c, Hongxia Zheng^a, Zhonghao Liu^{b,*}, Jinghui Hu^{b,**} , Jing Chen^{a,***} 

^a School of Pharmacy, Binzhou Medical University, Yantai, 264003, China

^b Yantai Engineering Research Center for Digital Technology of Stomatology, School of Stomatology, Binzhou Medical University, Yantai, 264003, China

^c Department of Thoracic Surgery, Binzhou Medical University Hospital, Binzhou, 256603, China

ARTICLE INFO

Keywords:

Cisplatin-resistant
Intracellular hypoxia
Program activation
Nanomedicine
Hypoxia activation

ABSTRACT

Cancer poses a significant threat to human life and health. Cancers treated with cisplatin invariably develop drug resistance. This challenge can be overcome by identifying and exploiting the vulnerabilities acquired by drug-resistant cancer cells, paving the way for finding effective novel treatment options for cisplatin-resistant cancers. Our previous study revealed that cisplatin resistance in cancer cells comes at the cost of increased intracellular hypoxia. In this study, we used 2-nitroimidazole modified hyaluronic acid (HA-NI) as the carrier. The cisplatin-resistant tumor cell specific intracellular hypoxia programmed activation nanomedicine (T/C@HN NPs) was constructed by the hypoxic toxic drug tirapazamine (TPZ) and encapsulating chlorin e6 (Ce6) into HA-NI using polymer assembly technology. The amphiphilic carrier could release free Ce6 molecules under the stimulation of intracellular hypoxic environment, and exhibit specific "activated state" photodynamic properties in cisplatin-resistant tumor cells. Upon irradiation, Ce6-mediated photodynamic therapy further intensifies hypoxia, amplifying its cytotoxicity. This project systematically evaluated the effects of T/C@HN NPs on the identification and recognition of cisplatin-resistant tumors using drug-resistant patient-derived xenograft (PDX) models. This study provides a promising avenue for the development of novel treatment of cisplatin-resistant tumors.

1. Introduction

Platinum-based anticancer drugs (cisplatin, carboplatin, and oxaliplatin) have been extensively used in the standard treatment of various solid malignant tumors [1,2], exhibiting favorable therapeutic efficacy during the initial stages of treatment and instilling hope in patients with cancer [3]. However, the non-specific distribution of chemotherapy agents often leads to systemic toxicity and adverse effects, and repeated chemotherapy can induce drug resistance in cancer cells [4–6]. This eventually culminates in chemotherapy failure [7–10]. Therefore, the development of novel therapeutic strategies specifically targeting

cisplatin resistance in tumors is of scientific importance and societal value [11].

Multidrug chemotherapy strategy is necessary to overcome cisplatin resistance in tumors [12–14]. Anticancer chemotherapy drugs with different mechanisms of action, such as cisplatin combined with paclitaxel, 5-fluorouracil and gemcitabine, can enhance the therapeutic effect on tumors [15,16]. However, combination chemotherapy usually causes severe toxicity and side effects [17,18]. Another strategy involves the use of nanocarriers for cisplatin transport [19]. Nanocarriers can circulate in the blood for longer periods, accumulate in tumor tissues through enhanced permeation and retention (EPR) effects, increase

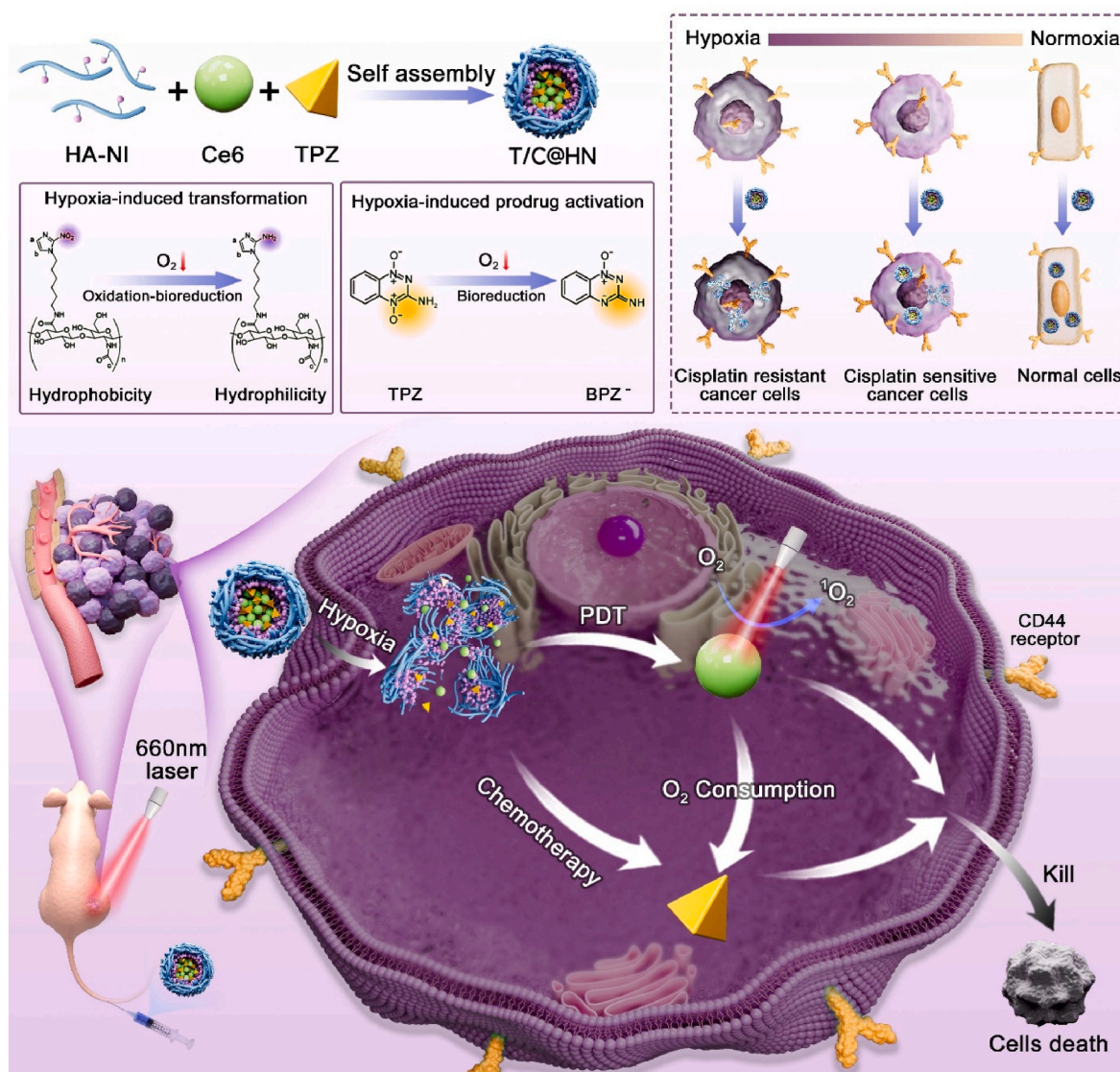
* Corresponding author.

** Corresponding author.

*** Corresponding author.

E-mail addresses: dentlzh@163.com (Z. Liu), bykfhjh@163.com (J. Hu), chenjingbyyxy@163.com (J. Chen).

¹ These authors contributed equally to this work.



Scheme 1. Schematic diagram of specific recognition of nanomaterials for cisplatin-resistant tumors. Nanomaterials release drugs by specific structural disintegration induced by intracellular hypoxia in cisplatin-resistant tumors. Free Ce6 can aggravate the cytotoxicity of TPZ by photodynamic therapy.

cellular uptake [20], and prevent platinum drug inactivation. Although nanocarriers have shown some success in overcoming cisplatin resistance, the limited EPR effect has significantly reduced its therapeutic efficiency [21]. Therefore, current strategies for overcoming cisplatin resistance in tumors are limited by major scientific challenges such as the emergence of new drug resistance and insufficient drug availability [22,23].

Tumor cells that have acquired chemotherapy resistance often undergo physicochemical changes that could be harnessed to overcome tumor resistance [24–26]. Bernard et al. found that drug-resistant melanoma cells harbored more reactive oxygen species (ROS) when compared with drug-sensitive cancer cells [27]. Considering this finding, they selected drugs that could increase ROS levels to treat drug-resistant melanoma, finally achieving better tumor suppression [28,29]. Therefore, the exploration and utilization of new characteristics and weaknesses of drug-resistant tumor cells can provide ideas for exploring new strategies to overcome drug resistance in tumors [30]. Warburg discovered the aerobic glycolysis effect in cancer cells, which states that cancer cells metabolize glucose into lactose to reduce oxygen consumption, even under oxygen-rich conditions [31–33]. Later, Gottesman et al. discovered the physiological characteristics of slower

glucose uptake and oxygen consumption rates in cisplatin-resistant tumor cells (compared to cisplatin-sensitive tumor cells) [34]. Hypoxia-inducible factor-1 α (HIF-1 α) is a major transcription factor that regulates hypoxia gene transcription and enzymes involved in glycolysis [35]. Fan et al. found that down regulating HIF-1 α levels can result in the overcoming of cisplatin resistance in cells [36]. Additionally, low oxygen levels in the tumor microenvironment affect various signaling pathways, such as DNA damage [37], mitochondrial activity, apoptosis, autophagy, and drug efflux, playing a crucial role in coordinating platinum-based chemotherapy resistance in clinical practice [38,39]. In our previous research, we hypothesized that there is a difference in oxygen content between cisplatin-resistant and cisplatin-sensitive tumor cells. We also conducted a preliminary investigation into the intracellular hypoxic state of platinum-resistant cancer cells [40]. It has been verified that the process of acquiring cisplatin resistance in tumor cells is accompanied by a new feature of intracellular oxygen deficiency at the single-cell level, which is expected to be a novel target for the treatment of cisplatin-resistant tumors [41].

Unlike normal tissues, solid tumors are typically hypoxic, which can hinder tumor treatment [42]. Therapeutic strategies developed for tumor tissue hypoxia are divided into three main categories:

intratumoral oxygen delivery, intratumoral oxygen generation, and intratumoral oxygen consumption strategy [43–45]. Among these approaches, oxygen-consuming therapeutic strategies are the most promising approach for treating hypoxic cisplatin-resistant tumors [46]. Oxygen-consuming agents (such as glucose oxidase, photosensitizers, and magnesium silicide) or vessel blockers are used to exacerbate the low-oxygen environment within the dense tumor microenvironment in combination with hypoxic anti-tumor prodrugs to induce cell death [47–49]. In a previous study, a hypoxia amplification nanomedicine was constructed to address hypoxia adaptive tolerance in tumor tissues [50], which activated the cytotoxicity of chemotherapy drugs and effectively cleared the tumors [51]. Promising results have been obtained in the treatment of hypoxia-adaptive tolerance in sensitive tumors [52]. However, there have been no studies on the therapeutic strategy of using intracellular hypoxia to suppress cisplatin-resistant tumors [52,53]. Utilizing the weakness of intracellular hypoxia to achieve specific recognition and kill cisplatin-resistant tumor cells is the key scientific problem addressed in this project.

Given the challenges of overcoming cisplatin-resistant tumors and improving therapeutic specificity, we developed a cascade of hypoxia-activated nanoparticles, taking advantage of the novel features of enhanced intracellular hypoxia in cisplatin-resistant tumor cells (Scheme 1). Using hydrophobic 2-nitroimidazole (NI) modified tumor-targeting hydrophilic hyaluronic acid (HA) as carrier, the photosensitizers chlorin e6 (Ce6) and the anoxic toxic drug tirapazamine (TPZ) were included. Programmed nanomaterials that could only be activated by hypoxia induced by cisplatin-resistant tumor cells were constructed by hydrophilic and hydrophobic self-assembly into nanomicelles. The hydrophobic NI of the amphiphilic carrier can be reduced to the hydrophilic 2-amino-imidazole in an intracellular hypoxic environment, which induces structural dissolution and drug release. The free photosensitizer Ce6 shows a specific "activation state" photodynamic property under 660 nm laser irradiation. Intracellular oxygen depletion was intensified by oxygen consumption, thereby activating the cytotoxicity of the chemotherapy drug TPZ. By harnessing intracellular hypoxia, we constructed an imaging-guided, programmed hypoxia activation therapy system that specifically targets and treats cisplatin-resistant tumors. This innovative approach enables the precise identification and targeted treatment of cisplatin-resistant tumors.

Abbreviations:

HA-NI	2-nitroimidazole modified hyaluronic acid
Ce6	chlorin e6
TPZ	tirapazamine
PDX	patient-derived xenograft
EPR	enhanced permeation and retention
NI	2-nitroimidazole
HA	hyaluronic acid
NI-NH-Boc	Boc-protected NI derivative
NI-D	NI derivative
EDCI	1-Ethyl-3-(3-dimethylaminopropyl) carbodiimide
NHS	N-Hydroxysuccinimide
¹ H NMR	Proton Nuclear Magnetic Resonance
FT-IR	Fourier Transform Infrared
MS	Mass Spectrometer
UV-Vis	Ultraviolet-Visible
Calcein AM	Calcein acetoxymethyl ester
PI	Propidium Iodide
DMSO	dimethyl sulfoxide
FBS	fetal bovine serum
CMC	critical micelle concentration
DLS	Dynamic light scattering
TEM	Transmission Electron Microscopy
DPBF	1,3-diphenylisobenzofuran
BEAS-2B	human normal lung bronchial epithelial cells
A549	human non-small cell lung cancer cells
A549 DDP	human non-small cell lung cancer cells with cisplatin resistance
CCK-8	cell counting kit 8

(continued on next column)

(continued)

CLSM	confocal laser scanning microscopy
DCFH-DA	2,7-dichlorodihydrofluorescein diacetate
PDT	photodynamic therapy
SCID	severe combined immune deficiency
H&E	Hematoxylin and Eosin
TUNEL	terminal deoxynucleotidyl transferase dUTP nick-end labeling
PBS	phosphate buffer saline
ANOVA	analysis of variance

2. Materials and methods

2.1. Synthesis and characterization of HA-NI

First, NI-D was prepared. NI (0.68 g, 6 mmol), and potassium carbonate (K₂CO₃, 1.68 g, 12 mmol) were dissolved in dimethyl Formamide (DMF). 6-(Boc-amino) hexyl bromide (1.68 g, 6 mmol) in DMF was then added dropwise and stirred at 80 °C for 4 h. Then, the reaction mixture was extracted with ethyl acetate. The organic layer was separated, dried over anhydrous sodium sulphate, and concentrated to obtain a yellow solid. The resulting product was added to a cold methanolic solution containing 1.25 M HCl and stirred at room temperature for 24 h. The solvent was removed from the reaction mixture using a rotary evaporator to obtain NI-D.

Next, NI-D was conjugated to HA. HA (0.4 g, 1.04 mmol) was added into phosphate buffer saline (PBS) (pH 6.0). Then, solutions of 1-Ethyl-3-(3-dimethylaminopropyl) carbodiimide (EDCI) (0.4 g, 2.08 mmol) and N-Hydroxy-Succinimide (NHS) (0.24 g, 2.08 mmol) were added under ice-cold conditions and stirred for 1 h. Subsequently, NI-D (0.16 g, 0.75 mmol) was added to the reaction mixture, and the pH was adjusted to 7.5. The mixture was stirred for 24 h. Following this, the resulting solution underwent dialysis first with a water/methanol mixture (1:1, V/V) for 24 h and then solely with water for another 24 h. HA-NI was obtained by freeze-drying.

To analyze and characterize the reaction products at each stage, Proton Nuclear Magnetic Resonance (¹H NMR), Fourier transform infrared (FT-IR, US), Mass Spectrometer (MS, 1290 InfinityII-6545XT, 1290 InfinityII-6545XT, SGP), and UV-Vis spectroscopy (DeNovix DS-11 FX+, US) were employed as the primary technique. The grafting rate of HA-NI was determined using UV-Vis spectroscopy at the peak of 325 nm.

2.2. Preparation and characterization of T/C@HN NPs

T/C@HN NPs were fabricated through a self-assembly procedure, wherein 10 mg of HA-NI was dissolved in 2 mL of water to initiate the preparation process. Four milliliters of 1 g/mL Ce6 chloroform solution and 2 mL of 1 g/mL TPZ chloroform solution were added to the HA-NI solution under conditions of ultrasonication. The combined solution underwent sonication at a power of 50 W for 8 min, utilizing an ultrasonic cell disruption device (Scientz-IID, sourced from China). Subsequently, all the chloroform was removed using a rotary evaporator. To eliminate any untrapped drug molecules, the mixture was subjected to ultrafiltration three consecutive times. Subsequently, the T/C@HN NPs were isolated by passing them through a 0.22 μm syringe filter, completing the preparation process. According to the above preparation method, T@HN NPs and C@HN NPs were prepared by adding only a chloroform solution of TPZ or only chloroform solution of Ce6. All prepared nanoparticle solutions were refrigerated at 4 °C for subsequent applications and analyses.

The TPZ concentration was quantified using the UV absorption at 460 nm, and the Ce6 concentration was quantified using the UV absorption at 660 nm. The drug-loading efficiency (L.E.) and drug-loading capacity (L.C.) were determined according to the following calculations: L.E. (%), expressed as a percentage, was calculated by dividing the

mass of the drug successfully loaded into the nanoparticles by the total mass of drug added initially, and then multiplying by 100.

L.C. (%), also presented as a percentage, was determined by dividing the mass of the loaded drug by the combined mass of all materials used in the nanoparticle formulation, followed by multiplying by 100.

The prepared nanomedicine was diluted 100 times with distilled water, after which 10 μ L was obtained for sample preparation, negatively stained with phosphotungstic acid (Solarbio, G1870), and the shape and structure of the nanoparticles were visualized by TEM (JEOL, JEM-1400, Japan). The particle sizes of the nanoparticles were measured using a DLS detector (Malvern Zetasizer ZS90, UK).

2.3. Hypoxia-responsive properties

NADPH (1.5 mg/mL) and $\text{Na}_2\text{S}_2\text{O}_4$ (0.3 mg/mL) were added to the PBS solution containing HA-NI and NI with the same concentration of NI to simulate an anoxic environment. NI characteristic absorption peak at 327 nm was estimated within 10 min using a UV-vis spectrophotometer.

2.4. Photodynamic and hypoxia amplification of T/C@HN NPs

Six microlitres 1.35 mg/mL DPBF solution, 20 μ L 0.5 mg/mL Ce6 solution and 5 % tween 20 were added to PBS solution to configure 1 mL experimental solution. The T/C@HN NPs+hypoxia+L group was incubated in an anoxic environment for 10 min prior to laser irradiation. Under irradiation with a 660 nm laser at 100 mW/cm², the UV-Vis absorption value of the solution at the peak of 410 nm was monitored every 1 min. Simultaneously, the changes in oxygen consumption within the solution was monitored using a portable oxygen-dissolving meter.

2.5. Cytotoxicity

To conduct toxicity assessments, 1×10^4 cells/well were seeded in a 96-well plate 24 h prior to the commencement of the experiment. Subsequently, the cells were exposed to fresh medium supplemented with compounds T/C@HN NPs+L or other formulations at different concentrations. The laser-related groups were exposed to a 660 nm laser after incubation for 12 h (100 mW/cm², 5 min). Following an additional 12 h of co-incubation, the viability status of the treated cells was quantitatively assessed utilizing the CCK-8 assay methodology.

2.6. Plate clonogenic assay

BEAS-2B, A549, and A549 DDP cells were seeded in three 6-well plates at a density of 5×10^3 cells/well. After 24 h of incubation, the cells were treated with fresh culture medium containing PBS, C@HN NPs, T@HN NPs, T/C@HN NPs, C@HN NPs+L, or T/C@HN NPs+L, the concentration of Ce6 was 0.54 μ M. The laser-related groups were exposed to a 660 nm laser after incubation for 12 h (100 mW/cm², 5 min). The culture medium was replaced with fresh blank medium every other day and incubated continuously for a week. The cells underwent washing with PBS, fixation in 4 % formaldehyde solution for 20 min, and subsequent staining with 0.01 % crystal violet dye for a duration of 30 min. Finally, images were captured. Quantitative statistics of the fluorescence signals were performed using ImageJ.

2.7. Cellular uptake of T/C@HN NPs

First, A549 DDP cells with a density of 1×10^5 cells/well were seeded in a glass-bottomed culture dish for 24 h. The cells were treated with fresh culture medium containing free Ce6 or T/C@HN NPs at 37 °C for 2 h, 6 h and 12 h, the concentration of Ce6 was 1 μ g/mL. Cells were fixed with paraformaldehyde and washed with cold PBS. Subsequently, images were collected using CLSM.

Then, BEAS-2B, A549, and A549 DDP cells with a density of 1×10^5 cells/well were seeded in a glass-bottomed culture dish for 24 h. The

cells were then treated with fresh culture medium containing free Ce6, T/C@HN NPs, or T/C@HN NPs+HA at 37 °C for 6 h, the concentration of Ce6 was 1 μ g/mL. In the T/C@HN NPs+HA treatment group, the cells were pretreated with HA (3 mg/mL) for 2 h and then co-incubated with T/C@HN NPs. Cells were fixed with paraformaldehyde and washed with cold PBS. Subsequently, images were collected using CLSM. The fluorescence signals of Ce6 in BEAS-2B, A549, and A549 DDP cells co-cultured with T/C@HN NPs for 6 h under hypoxic conditions were obtained in an anaerobic incubator (GC-CT, CHN) using a similar method.

2.8. Detection of live/dead cells

A549 DDP cells with a density of 1×10^5 cells/well were seeded in a glass-bottomed culture dish for 24 h. Subsequent to the incubation period, the cells were introduced to a new medium comprising of PBS, C@HN NPs, T@HN NPs, T/C@HN NPs, C@HN NPs+L, or T/C@HN NPs+L, each containing an equivalent Ce6 concentration of 0.54 mM. The laser-related groups were exposed to a 660 nm laser after incubation for 12 h (100 mW/cm², 5 min). After co-incubation for another 12 h, the cells were treated with Calcein Acetoxymethyl ester (Calcein AM) and Propidium Iodide (PI) for 30 min. Ultimately, the cells underwent multiple rinses with PBS and were subsequently visualized through the application of CLSM.

2.9. Apoptosis assays

A549 DDP cells with a density of 1×10^5 cells/well were seeded in 6-well plates and co-incubated for 24 h. Replace the culture medium with fresh culture medium containing PBS, C@HN NPs, T@HN NPs, T/C@HN NPs, C@HN NPs+L, or T/C@HN NPs+L at a Ce6 equivalent concentration of 0.54 μ M. The laser-related groups were exposed to a 660 nm laser after incubation for 12 h (100 mW/cm², 5 min). After co-incubation for another 12 h, wash the tumor cells with PBS and perform trypsin digestion. Detect apoptosis through double staining with Annexin V-FITC/PI using flow cytometry.

2.10. Intracellular ROS level

A549 DDP cells with a density of 1×10^5 cells/well were seeded in a 35 mm confocal glass bottom-dish and co-incubated for 24 h. The cells were treated with fresh medium containing PBS, C@HN NPs, T@HN NPs, T/C@HN NPs, C@HN NPs+L or T/C@HN NPs+L at a Ce6 equivalent concentration of 0.54 μ M. The laser-related groups were exposed to the 660 nm laser after incubation for 12 h (100 mW/cm², 5 min). DCFH-DA was added to a confocal dish and incubated at 37 °C for 30 min. After washing with PBS, intracellular ROS generation was examined using a fluorescence microscope.

2.11. Establishment of the PDX model

With the endorsement from the Ethics Committees of both the Second Affiliated Hospital of Guangzhou Medical University (Guangzhou, China, SYXK 2018-0192) and Binzhou Medical University (Yantai, China, 2022-037), freshly excised lung cancer tumors originating from patients were procured for research purposes. Related experiments should be conducted in accordance with relevant ethical regulations. Informed consent was obtained from all the patients before specimen collection. The tumor tissues were cut into small pieces and placed into cryovials, which were then frozen in liquid nitrogen tanks. The cryoprotectant utilized was a blend of 10 % dimethyl sulfoxide (DMSO) and 90 % fetal bovine serum (FBS), formulated specifically for the purpose of freezing. SCID mice received transplants of tumor fragments, each measuring $2 \times 2 \times 2$ mm³ in volume, into their left hind legs. After at least three generations of transmission, a PDX model was established by subcutaneous implantation of the tumor tissue into the legs of nude mice.

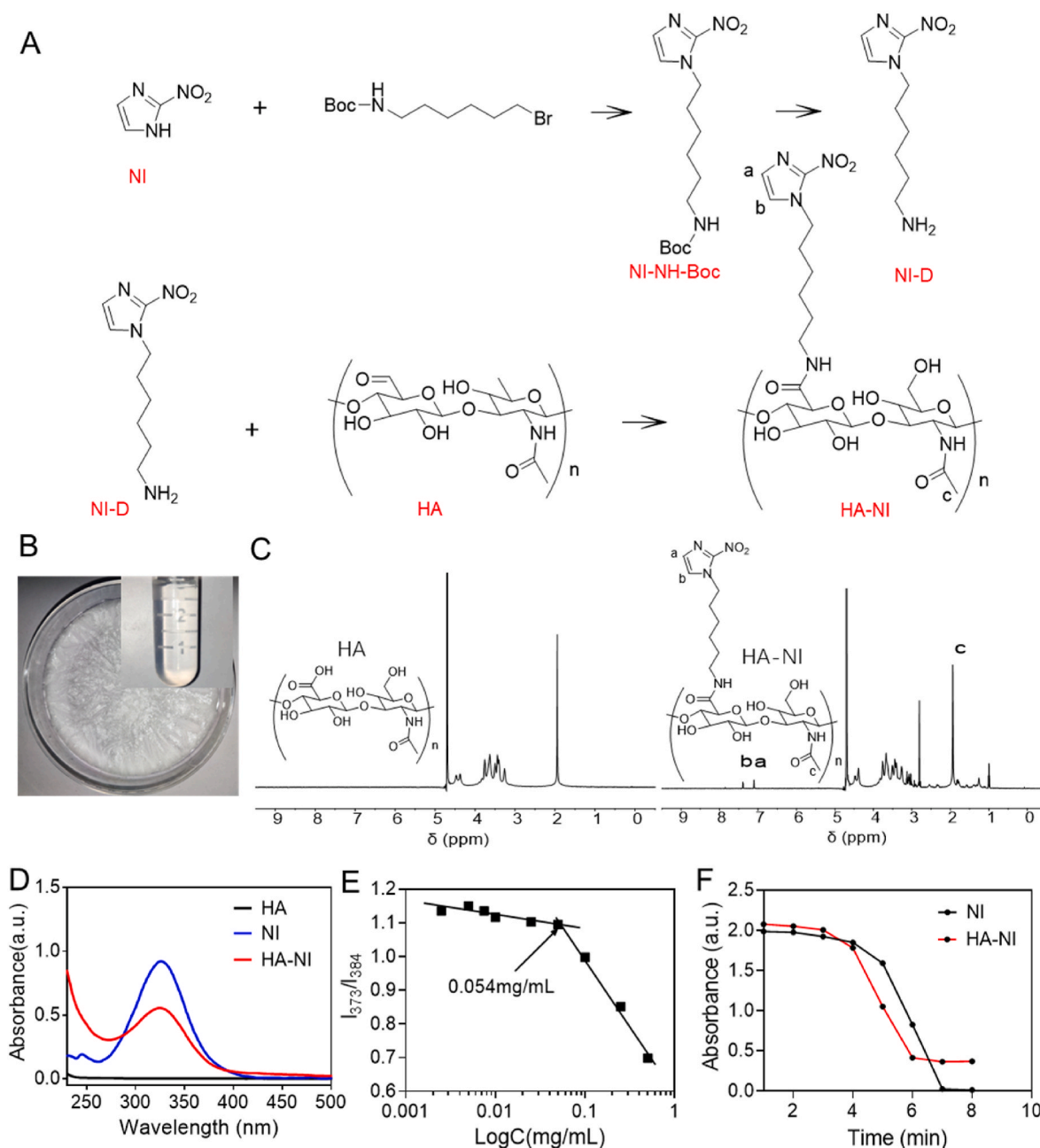


Fig. 1. Preparation and characterization of HA-NI. A) Synthetic scheme of HA-NI conjugates. B) The solid and solution morphology of HA-NI. C) The ^1H NMR spectra of HA and HA-NI. D) Ultraviolet visible absorption spectra of HA, NI, HA-NI. E) Plot of I_{373}/I_{384} intensity versus concentrations of HA-NI. F) The characteristic UV absorption values of NI and HA-NI at 327 nm under hypoxic conditions.

2.12. *In vivo* anti-tumor efficacy in PDX models

Once the tumor volume attained approximately 100 mm^3 , the tumor-bearing mice underwent injection with varying formulations via the tail vein at an interval of one day. The dosages of Ce6 and TPZ were 2 and 0.85 mg/kg, respectively. The monitoring of both tumor volume and mice body weight is imperative for accurate assessment and documentation. The calculation of tumor suppression rate was performed as outlined below:

$$\text{Tumor volume} = \text{length} * \text{width}^2 / 2.$$

$\text{Tumor inhibition rate (\%)} = (\text{mean tumor volume in control group} - \text{tumor volume in treatment group}) / \text{mean tumor volume in control group}.$

Tumors and major organs were collected for further examination after treatment. All tumor tissues were photographed and weighed.

2.13. Cells lines and animals

BEAS-2B, A549 cells and A549DDP cells were purchased from the Cell Resource Center (Procell Life Science & Technology Co., Ltd., China) and were cultured in DMEM medium (Wisent Biotechnology Co., Ltd., China) supplemented with 10 % fetal bovine serum (FBS, Gibco, US) and 1 % penicillin and streptomycin (PS, Procell Life Science & Technology Co., Ltd., China). All cells were maintained at 37°C and 5 % CO_2 . BALB/c nude mice (female, 6 weeks old) were purchased from GemPharmatech Co., Ltd. (China). All animals were treated according to the Guide for the Care and Use of Laboratory Animals and all procedures were approved by the Animal Experimentation Ethics Committee of Binzhou Medical University (2022-037).

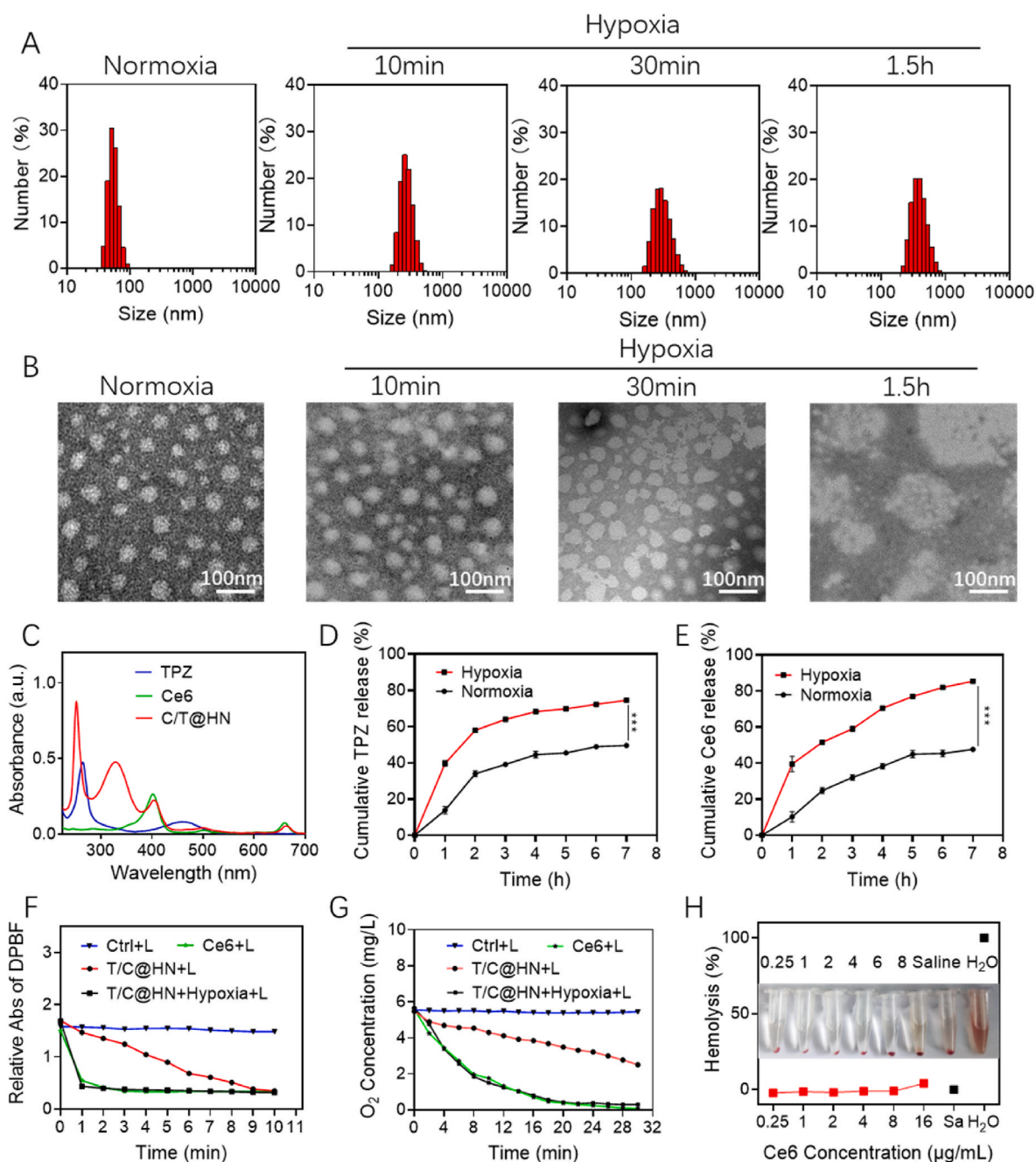


Fig. 2. Preparation and characterization of T/C@HN NPs. A) Representative DLS images showcase T/C@HN NPs under normal conditions and after incubation for 15, 30 min, and 1.5h in hypoxic setting. B) Representative TEM images showcase T/C@HN NPs under normal conditions and after incubation for 15, 30 min, and 1.5h in hypoxic setting. Scale bar, 100 nm. C) The UV absorption curve of TPZ, Ce6 and T/C@HN NPs. D) Release curve of TPZ in T/C@HN NPs in normal setting and in hypoxia setting. E) Release curve of Ce6 in T/C@HN NPs in normal setting and in hypoxia setting. F) The trend of changes in the UV absorption values of DPBF at 410 nm in different groups. G) The oxygen change curves in different groups detected by a portable dissolved oxygen analyzer. H) Hemolysis rate and corresponding images of distilled water, saline and T/C@HN NPs with different concentrations. $***P < 0.001$.

2.14. Statistical analysis

Data are presented as mean \pm s.d. Student's t-test was used for the statistical comparison between the two groups. One-way analysis of variance (ANOVA) with a Tukey multiple comparisons test was used for statistical comparison among multiple (more than two) groups. Differences are considered statistically significant at the level of $P < 0.05$. Significant differences are indicated by * $P < 0.05$; ** $P < 0.01$; *** $P < 0.001$; **** $P < 0.0001$.

3. Results and discussion

3.1. Preparation and characterization of HA-NI

The amphiphilic carrier HA-NI was synthesized using the synthetic circuit in Fig. 1A. NI was first alkylated with 6- (Boc amino)-hexyl bromide to obtain a Boc-protected NI derivative (NI-NH-BOC). The amino groups in NI-NH-Boc were deprotected in an acidic environment to produce an NI derivative (NI-D).

Fourier transform infrared (FT-IR) spectroscopy was used to characterize NI-NH-Boc and NI-D. Comparison of the infrared spectra of NI-

NH-Boc and NI-D revealed that the stretching vibration peak of C=O in the amide bond at 1693 cm^{-1} disappeared after the reaction, and a new stretching vibration peak of -NH_2 was introduced at 1662 cm^{-1} , indicating the successful synthesis of NI-D (Fig. S1A). ^1H NMR spectroscopy was used to further verify the chemical structure of NI-D. As shown in Fig. S1B, the proton peak of c-i confirmed that the intermediary NI-NH-D has been successfully synthesized, and the disappearance of methyl proton peak at $\delta 1.30$ confirmed the successful protection of Boc group, thus confirming the synthesis of NI-D. Since -NO_2 in NI has an Ultraviolet-Visible (UV-Vis) absorption peak at 327 nm, and the absorption of NI and NI-D was detected using UV-Vis spectrophotometry. As shown in Fig. S1C, both NI and NI-D exhibited maximum characteristic absorption wavelengths at 327 nm. The theoretical molecular weight of NI-D is 212.13, and the mass spectrum result was 213.10, combining the molecular weights of one proton and consistent with the theoretical molecular weight (Fig. S1D).

Subsequently, NI-D was amidated with HA, which was activated using EDC and NHS to produce HA-NI. The synthesized carrier exhibited a white flocculent appearance after freeze-drying, became transparent and evenly dispersed when dissolved in water (Fig. 1B). ^1H NMR spectroscopy was used to verify the chemical structure of HA-NI. As shown in Fig. 1C, there were two additional proton peaks on the imidazole ring of HA-NI, indicating that NI was successfully grafted onto HA. According to the UV-Vis spectroscopy results in Fig. 1D, the UV spectrum of HA-NI exhibits a distinct NI absorption peak centered at 327 nm, which further confirms that NI was successfully grafted onto the HA-NI sample. The grafting rate of NI in HA-NI was calculated to be 9.18 %, based on the characteristic UV absorption peaks of NI (Fig. S2).

Polymer micelles used to load drugs experience extreme dilution after injection into the vein. The stability of polymer micelles can be characterized by their critical micelle concentration (CMC) [54,55]. A smaller CMC value of micelles is a crucial parameter, indicating a stronger ability to maintain their structural integrity after dilution. This is essential for preventing premature leakage of loaded drugs. We used pyrene as a model drug for CMC determination in HA-NI carriers. When the polymer reached the critical micelle concentration, the environment of pyrene entering the micelle changed in polarity, and the corresponding I_{373}/I_{384} mutation also occurred. As depicted in Fig. 1E, the CMC value of micellar HA-NI was 0.054 mg/mL, indicating that the HA-NI carrier had good anti-dilution ability. Due to the presence of the nitroimidazole structure in HA-NI, it changes to an amino structure under hypoxic conditions. Therefore, we simulated a hypoxic environment using $\text{Na}_2\text{S}_2\text{O}_4$ and observed the changes in UV absorption with the extension of hypoxia. As shown in Fig. 1F and Fig. S3, the UV absorption values of NI and HA-NI at 327 nm exhibited a significant reduction after 4–6 min of hypoxia, indicating that the hypoxia response performance of NI grafted onto HA remained good.

3.2. Preparation and characterization of T/C@HN NPs

We developed a nanodrug delivery system (T/C@HN NPs) using HA-NI polymer micelles as carriers that encapsulated Ce6 and TPZ through ultrasonic self-assembly. To achieve the optimal synergistic therapeutic effect of the two drugs, we conducted a screening of the mass ratio for the administration of TPZ and Ce6. As illustrated in Fig. S4, when the mass ratio of TPZ to Ce6 is 2:1, the combination index of the drugs is less than 1, indicating a synergistic effect between the two drugs. Furthermore, this ratio exhibits the best synergistic therapeutic effect compared to other groups. Therefore, the mass ratio of TPZ to Ce6 was fixed at 2:1 for subsequent experiments.

First the morphology and particle size of the nanomedicines were evaluated under normoxic conditions. The hydrodynamic diameter of T/C@HN NPs was determined to be 54.0 nm by Dynamic light scattering (DLS) analysis (Fig. 2A). The prepared T/C@HN NPs can be stably stored in FBS serum or PBS over an extended period without undergoing aggregation or degradation within a short timeframe (Fig. S5).

Transmission electron microscopy (TEM) confirmed that the nanomedicine had a spherical structure and uniform particle size (Fig. 2B). The UV absorption curve showed that both TPZ and Ce6 characteristic absorption peaks were present in the T/C@HN NPs, confirming the successful encapsulation of the nanomedicine (Fig. 2C). The drug loading and encapsulation efficiencies of TPZ and Ce6 in nanomedicines were calculated based on their characteristic UV absorption peaks (Fig. S6). The results showed that the loading efficiency and drug loading capacity in nanomedicine were 53.5 % and 12.9 % for Ce6, and 44.1 % and 5.5 % for TPZ, respectively.

Next, we systematically analyzed and verified the hypoxia-responsive performance of the T/C@HN NPs. Under hypoxic conditions, the DLS results in Fig. 2A revealed a gradual increase in the particle size and broadening of the particle size distribution range of the nanomedicine with increasing hypoxic time, indicating a deterioration in dispersibility. The TEM images further confirmed that hypoxia caused the regular spherical drug particles to gradually expand and rupture with blurred boundaries, disintegrating the nanoparticle structure (Fig. 2A). Hypoxia-responsive carriers can achieve the controlled release of nanomedicines. We compared the *in vitro* release of the nanomedicines under normoxic and hypoxic conditions. As shown in Fig. 2D and E, the drugs encapsulated in the nanoparticles exhibited higher release levels and faster release rates under hypoxic conditions. The release rate of TPZ increased from 49.6 % to 74.5 % under hypoxia after 8 h of incubation, which was 24.9 % higher than the drug release rate under normoxic conditions. The release rate of Ce6 increased from 47.4 % to 85.4 % under hypoxia, which was 38.0 % higher than the drug release rate under normoxic conditions. This provides a reliable basis for the higher release of nanomedicines from hypoxic tumor cells and the hypoxic environment of solid tumors. Photodynamic properties of nanomedicines can be achieved using laser irradiation. As shown in Fig. S7, the characteristic absorption peak at 660 nm decreased with increasing laser irradiation time in a power-dependent manner. To verify the rapid activation of the photodynamic properties of nanomedicines under hypoxic conditions, 1,3-Diphenylisobenzofuran (DPBF) was first used as a probe for singlet oxygen to detect photodynamic performance. The UV absorption of DPBF at 410 nm rapidly decreased when the T/C@HN NPs were irradiated with a laser for 1 min under certain low-oxygen conditions, showing almost the same trend as the free Ce6 group. However, in T/C@HN NPs irradiated with laser for 1 min under normoxic conditions, the UV characteristic absorption peak of DPBF slowly decreased and eventually reached a level similar to that of the T/C@HN NPs irradiated with the laser for 1 min under certain low-oxygen conditions. This may be due to the encapsulation of Ce6 in the NPs, which cannot be well dispersed, resulting in aggregation quenching and reduced photodynamic performance (Fig. 2F). A portable oxygen analyzer monitored alterations in oxygen levels in the nanomedicine solution subsequent to 30 min of 660 nm laser irradiation at 100 mW/cm^2 power. The oxygen content of the T/C@HN NPs pre-incubated under hypoxic conditions decreased rapidly within 5 min of laser irradiation. However, under normal oxygen conditions, the oxygen content in the T/C@HN NPs solution decreased at a relatively slow rate. This indicates that hypoxia accelerates the rapid photodynamic performance of the T/C@HN NPs, leading to amplified hypoxia (Fig. 2G). To conduct *in vivo* experiments, the hemolytic properties of the nanomedicine were validated. The hemolysis rate was less than 5 % when the concentration of Ce6 in T/C@HN NPs was in the range of 0–16 $\mu\text{g/mL}$, which proved that no hemolysis occurred in this concentration range indicating good biological safety (Fig. 2H).

3.3. Evaluation of T/C@HN NPs specific recognition and inhibition of cisplatin resistant tumor cells

Based on the above verification, the prepared T/C@HN NPs exhibited efficient photodynamic properties activated by low oxygen levels. Our previous study revealed that drug-resistant cells have a lower

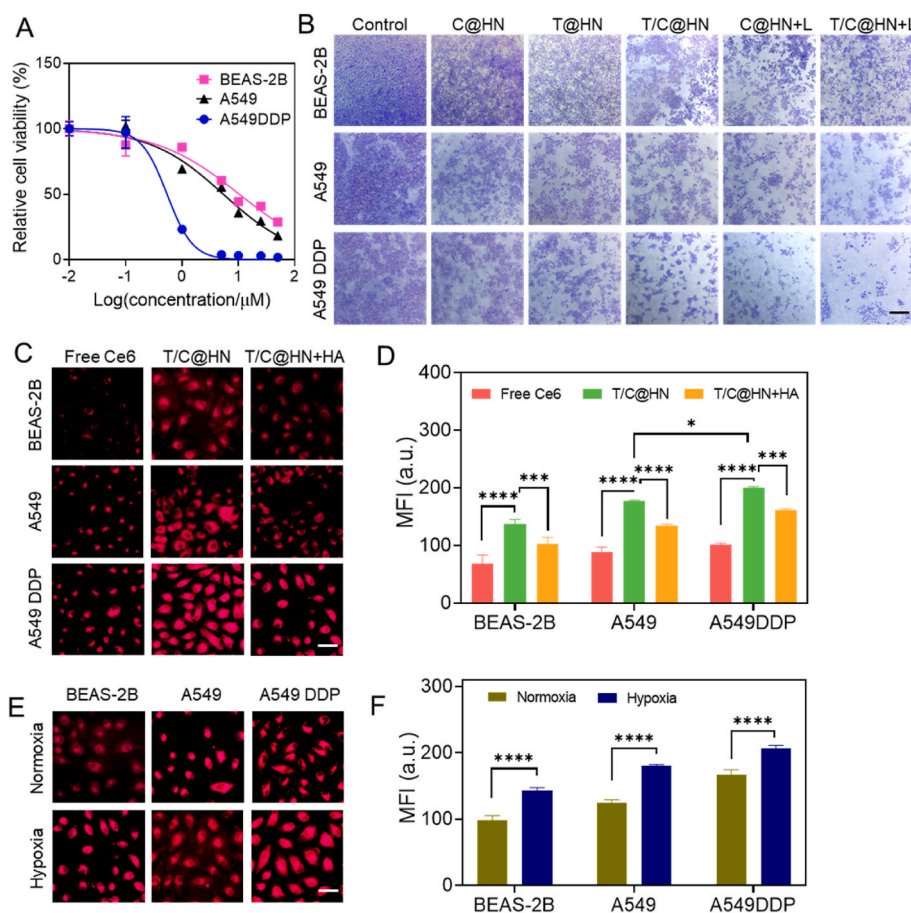


Fig. 3. The inhibitory effect and mechanism of T/C@HN NPs on three types of cells. A) Viability of BEAS-2B, A549 and A549 DDP cells treated with T/C@HN NPs+L for 6 h. B) One-week analysis of colony formation by nanoparticles on BEAS-2B, A549, and A549 DDP cell proliferation post-treatment with control, C@HN NPs, T@HN NPs, T/C@HN NPs, C@HN NPs+L and T/C@HN NPs+L. Scale bar, 500 μm . C) The fluorescence signals of Ce6 in BEAS-2B, A549 and A549 DDP cells co-cultured with different formulations for 6 h. D) Quantitative analysis of the red fluorescence signal of Ce6 in C. E) The fluorescence signals of Ce6 in BEAS-2B, A549 and A549 DDP cells co-cultured with T/C@HN NPs for 6 h under normoxic and hypoxic conditions. F) Quantitative analysis of the red fluorescence signal of Ce6 in E. Scale bar, 40 μm . Error bars represent \pm s.d. Statistical significance was determined by two-way ANOVA (B and D). * $P < 0.1$, *** $P < 0.001$, **** $P < 0.0001$.

degree of intracellular hypoxia compared to sensitive tumor cells [41]. Therefore, we predicted that nanomedicines would have the ability to specifically recognize and inhibit cisplatin-resistant tumor cells. Three cell lines, human normal lung bronchial epithelial cells (BEAS-2B), human non-small cell lung cancer cells (A549), and human non-small cell lung cancer cells with cisplatin resistance (A549 DDP) were selected to evaluate the inhibitory effect of T/C@HN NPs, those oxygen content gradually decreased [56]. Quantification of cell viability using a cell counting kit 8 (CCK-8) assay confirmed that T/C@HN NPs+L exhibited the strongest inhibition rate against A549 DDP (Fig. 3A). The IC_{50} values of T/C@HN NPs+L for BEAS-2B, A549, and A549 DDP cells were calculated as 10.38 μM , 5.41 μM and 0.54 μM , respectively. The plate cloning method was used to further evaluate the inhibitory effects of different nanomedicines on the three cell types. As shown in Fig. 3B, compared with other groups, A549 DDP cells treated with T/C@HN+L had the smallest cell population, whereas BEAS-2B cells treated with T/C@HN+L showed almost no decrease in cell population, indicating that the nanodrug has strong selectivity for cisplatin-resistant tumors and minimal effect on normal cells.

The endocytosis of T/C@HN NPs at different times in A549 DDP cells was validated at first to investigate the mechanism of T/C@HN NP-specific recognition of cisplatin-resistant cells. The number of nanomedicine entering cells was quantified using the Ce6 fluorescence signal via confocal laser scanning microscopy (CLSM). As shown in Fig. S8, increased incubation time enhanced the intensity of red fluorescence signals in the cytoplasm of A549 DDP cells gradually increased,

indicating that the endocytosis of the nanomedicines was time-dependent. Compared with the free Ce6 group, T/C @ HN NPs showed stronger signals in the cells, indicating that the carrier facilitated the endocytosis of the nanomedicine.

We then investigated the intracellular uptake of the nanomedicine at 6 h in BEAS-2B, A549, and A549 DDP cells, and found that the fluorescence signal in A549 DDP cells was significantly higher than that in A549 and BEAS-2B cells (Fig. 3C and D). HA enters cells through CD44 receptors expressed in cells [55–58]. Therefore, we first cocultured HA with cells to saturate the receptors that mediate HA endocytosis. As depicted in Fig. 3C and D, the red fluorescence intensity decreased in all three cell lines, indicating that all three cell lines expressed HA transporter receptors and were subject to competition from external HA to reduce the internalization of the nanomedicine. Due to the hypoxic responsiveness of the nano drug carrier we prepared and the varying oxygen levels among the above three cell types, we predict that the differences in intracellular drug fluorescence signals may be caused by differences in oxygen levels. We validated the fluorescence signals of the T/C@HN NPs in the three cell types under normoxic and hypoxic conditions. An increase in the intensity of red fluorescent signals was observed by creating a hypoxic environment using a hypoxia incubator (Fig. 3E and F). This phenomenon is mainly attributed to the hypoxia responsive nanomedicine undergoing dissociation, which alleviates the fluorescence quenching encapsulated in the nanomedicine. The release of a large amount of Ce6 is conducive to the realization of Ce6 photodynamic performance and the activation of TPZ cytotoxicity. Owing to

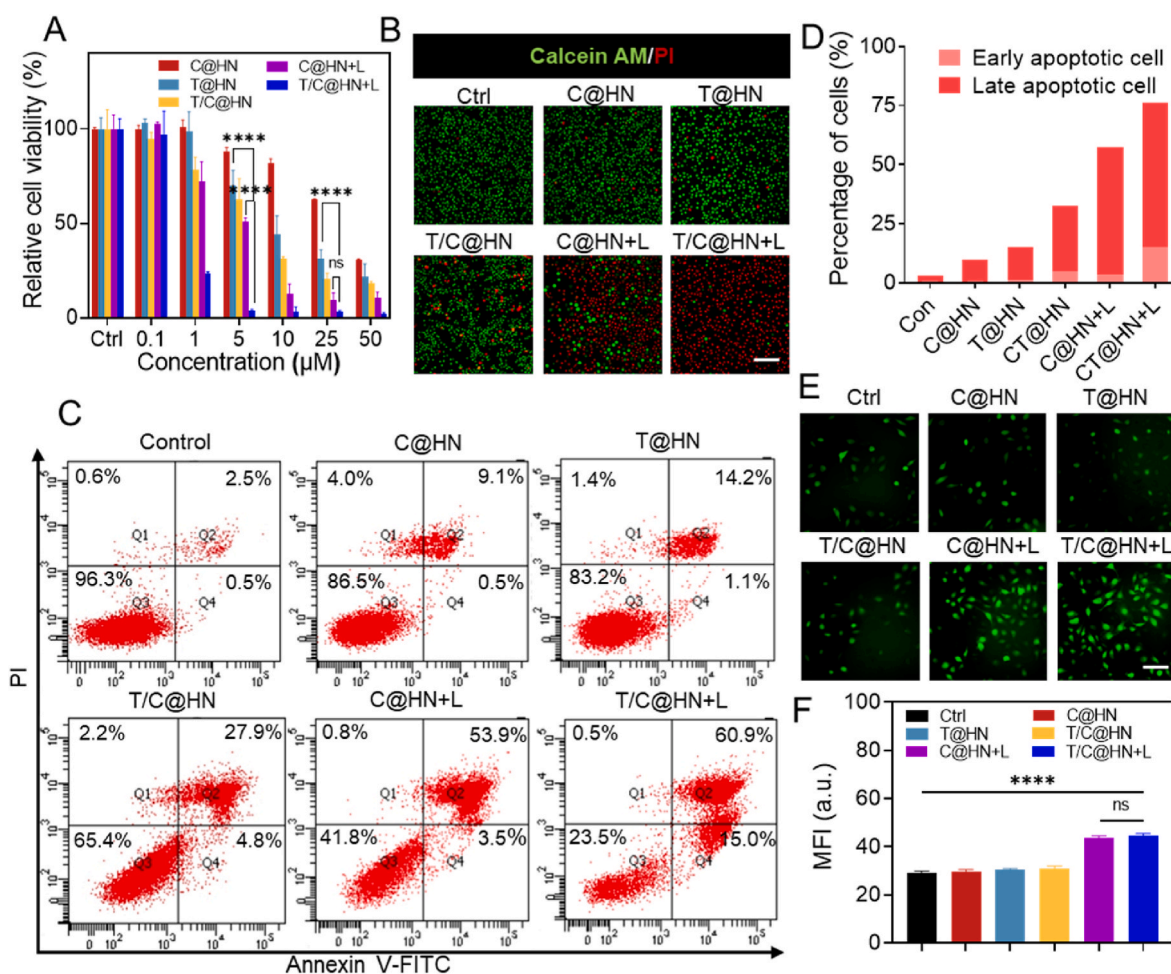


Fig. 4. *In vitro* inhibition evaluation of T/C@HN NPs on A549 DDP cells. A) The viability of A549 DDP cells determined by CCK-8 after 24 h incubation with different concentrations and formulations. B) CLSM images of A549 DDP cells co-stained with calcein AM and propidium iodide (PI) after treatment with different formulations at a Ce6 equivalent concentration of 0.54 μM. Scale bars, 200 μm. C) A549 DDP cell apoptosis detected by Annexin V-FITC and PI double staining after treatment with different formulations at a Ce6 equivalent concentration of 0.54 μM. D) Quantification of early and late apoptosis of A549 DDP cell in C. E) Detection of ROS production by DCFH-DA in A549 DDP cells after different treatments at a Ce6 equivalent concentration of 0.54 μM. F) Quantification of the green fluorescence intensity of DCFH-DA staining in E. Scale bars, 100 μm. Error bars represent ± s.d. Statistical significance was determined by one-way ANOVA (A) or Student's t-test (F). **** $P < 0.0001$, ns $P > 0.05$.

the highest degree of hypoxia exhibited by A549 DDP cells among the three cell types, the fluorescence signal intensity of T/C@HN NPs within A549 DDP cells was the strongest and showed the best *in vitro* inhibitory effect, which corresponds to the results in Fig. 3A–D.

3.4. *In vitro* inhibition evaluation of T/C@HN NPs on A549 DDP cells

In order to facilitate better *in vivo* treatment with T/C@HN NPs, we validated their ability to inhibit the growth of cisplatin-resistant tumor cells on A549 DDP cells *in vitro*. Initially, the intracellular hypoxia levels of A549DDP cells were evaluated using a hypoxia assay kit, confirming the potent photodynamic therapy (PDT) effect induced by laser irradiation. The results showed that the oxygen content in A549DDP cells treated with T/C@HN NPs under laser irradiation was significantly reduced (Fig. S9). The cascade effect can activate prodrugs that respond to hypoxia, thereby synergistically enhancing chemotherapy efficacy. The cytotoxicity of the nanomedicine against A549 DDP cells was determined using a CCK-8 assay. Fig. 4A demonstrates that the combination of T/C@HN NPs with laser irradiation showed the highest killing effect on tumor cells compared to the survival rate of cells in other groups. This indicates that the programmed activation nanosystem, combining photodynamic therapy and hypoxia-triggered chemotherapy, effectively reversed cisplatin resistance in tumors. The IC_{50}

value of T/C@HN NPs+L with high cytotoxicity was 0.54 μM Ce6, while the IC_{50} values of C@HN NPs+L and T/C@HN NPs were as high as 3.30 μM and 10 μM Ce6, respectively. A live/dead staining kit was used to visually observe the viability of the cells using CLSM. Consistent with the quantitative results above, almost all A549 DDP cells incubated with T/C@HN NPs and irradiated with a laser showed strong red fluorescence (indicating cell apoptosis), whereas the other treatment groups still showed green-fluorescent cells (indicating cell survival) (Fig. 4B). In addition, flow cytometry was used to evaluate the extent of A549 DDP cell apoptosis induced by T/C@HN NPs. As shown in Fig. 4C and D, incubation with C@HN NPs and T@HN NPs induced apoptosis in less than 20 % while C/T@HN NPs reach to 32.7 % of A549 DDP cells. Incubation with C@HN NPs followed by laser irradiation increased the apoptosis rate of A549 DDP cells to 57.4 %. Then, treatment with T/C@HN NPs followed by laser irradiation resulted in the highest percentage of apoptotic cells up to 75.9 %. Finally, 2,7-dichlorodihydrofluorescein diacetate (DCFH-DA) was selected as a fluorescent ROS probe to visualize cellular ROS generation during photodynamic therapy (PDT). The fluorescence intensity was significantly higher in C@HN+L and T/C@HN+L NPs groups compared to the others, indicating that the encapsulated Ce6 had a strong PDT effect. Notably, the intensity of the ROS fluorescence produced by the T/C@HN NPs in combination with laser irradiation in the treatment group was 1.54-fold higher than that in

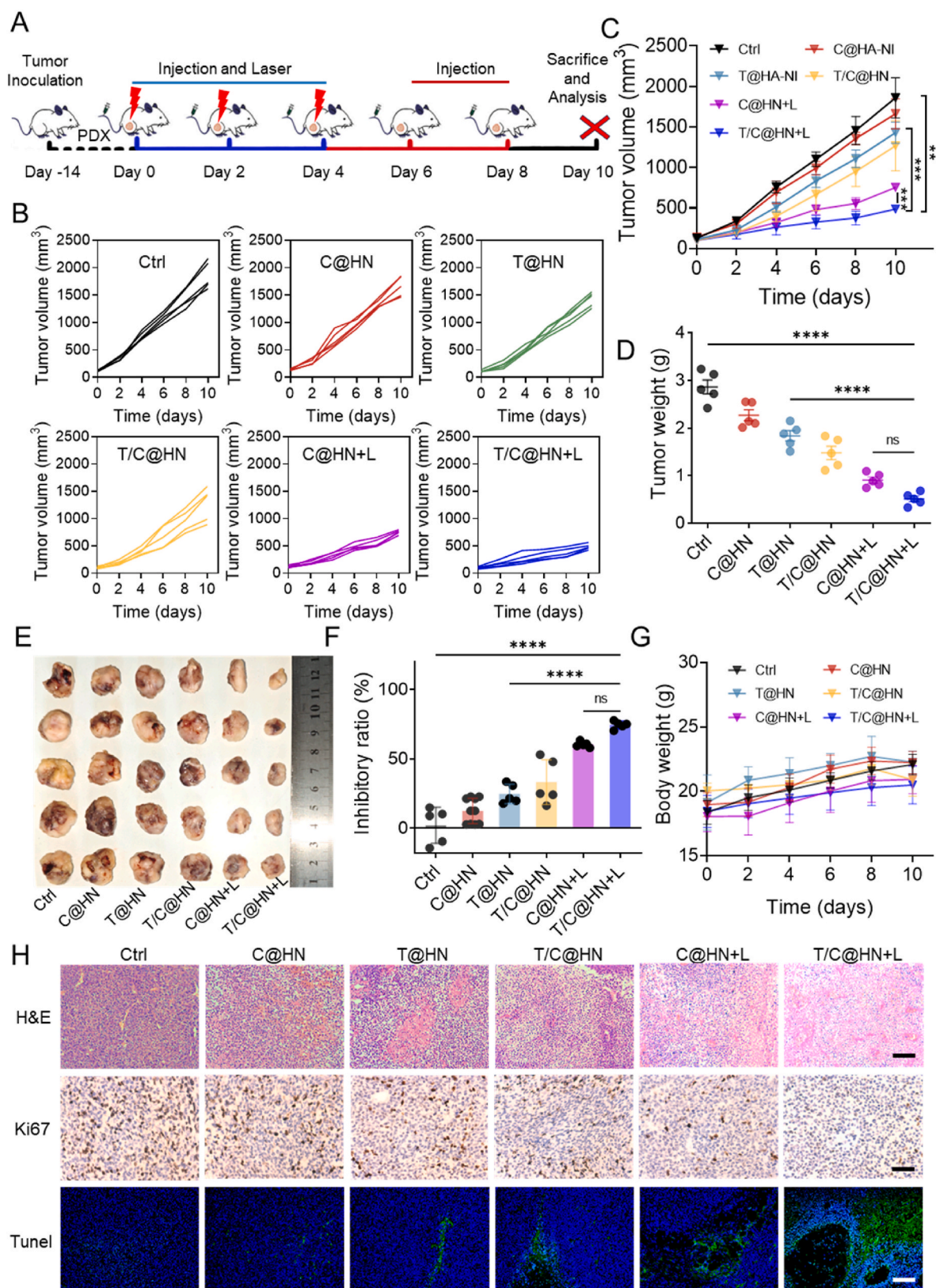


Fig. 5. Specific inhibition efficacy of T/C@HN NPs in nude mouse bearing PDX model. A) Schematic diagram of *in vivo* anti-tumor experiments. B) PDX tumor growth kinetics of each BALB/c nude mice in different treatment groups. C) Statistical analysis of tumor growth curves in mice. D) Tumor weight collected from mice in different treatment groups. E) Tumor images collected from mice. F) Tumor inhibition rates in different treatment groups. G) Body weight changes in mice of the six treatment groups. H) Staining of tumor tissue sections obtained from mice after treatment, including H&E, Ki67 and TUNEL. Scale bar, 100 μ m, 50 μ m, 100 μ m respectively. Error bars represent \pm s.d. Statistical significance was determined by Student's t-test (C, D and F). $**P < 0.01$, $***P < 0.001$, $****P < 0.0001$, ns $P > 0.05$.

the control group (Fig. 4E and F). The *in vitro* experimental results confirmed that T/C@HN NPs with laser have a strong inhibitory effect on cisplatin resistant cell A549 DDP through the programmed activation of photodynamic therapy and chemotherapy by intracellular hypoxia.

3.5. Evaluation of *in vivo* specific inhibition of PDX tumor model

The tumor tissues from patients preserve a relatively complete clinical tumor microenvironment, which is considered a more authentic model for *in vivo* anti-tumor research in animals. The PDX model was established by subcutaneously implanting tumor tissue from patients into the legs of nude mice, which were passed down from generation to generation in severe combined immune deficiency (SCID) mice. This kind of tumor tissue is highly malignant and has a high degree of drug resistance. When the tumor volume reached approximately 100 mm³, the nude mice were evenly divided into six groups and injected with the predetermined nanomedicine through the tail vein every other day, according to the treatment plan shown in Fig. 5A. The dose for each administration was based on an equivalent concentration of 2 mg/kg. In the treatment group, which required laser irradiation, a 300 mW/cm² 660 nm laser was irradiated for 5 min after 4 h of administration. Tumor volume was monitored daily throughout the treatment process. The rapid increase in tumor volume from 100 mm³ to 2000 mm³ within 10 days in the control group indicated a high degree of malignancy in this PDX model (Fig. 5B and C). Tumors in the C@HN NPs, T@HN NPs, T/C@HN NPs, and C@HN NPs+L treatment groups were inhibited to varying degrees, with the T/C@HN NPs+L treatment group showing the greatest degree of tumor inhibition. After 10 days of treatment, the tumors were dissected, weighed, and photographed. The results were consistent with the tumor inhibition curve (Fig. 5D and E). The average tumor inhibition rate of T/C@HN NPs+L group was calculated to be 74.2 %, which was much higher than that of other groups, indicating that PDT combined with chemotherapy had a strong and effective tumor inhibition effect (Fig. 5F). Notably, the body weight of the mice was maintained at a normal level and increased slightly, indicating that the nanomedicine has specificity for tumors and can reduce systemic toxic side effects (Fig. 5G). Hematoxylin and eosin (H&E) staining of mouse tumor slices were conducted to evaluate the tumor treatment status. As shown in Fig. 5H, the number of tumor cell nuclei in the T/C@HN+L NPs group was significantly reduced, indicating tumor tissue necrosis. The Ki67 staining results indicated that the tumor tissue in the T/C@HN+L NPs treatment group almost lost its proliferative ability (Fig. 5H). In addition, a large amount of green fluorescence signals were observed in the terminal deoxynucleotidyl transferase dUTP nick-end labeling (TUNEL) results, indicating that the T/C@HN+L NPs maximally promoted tumor tissue apoptosis (Fig. 5H).

To further evaluate the *in vivo* safety of the nanomedicine, we collected serum samples from the treated mice for blood biochemical analysis. The results showed that the biochemical indicators were within the normal range (Fig. S10). H&E staining was used to analyze the pathological changes in the main organs, such as the heart, liver, spleen, lung, and kidney of the mice (Fig. S11). The results showed that the drug did not cause significant damage to the organs, indicating that hypoxia-activated programmed nanomedicine is biologically safe.

4. Conclusions

In this study, a programmable activated nanosystem was prepared by encapsulating Ce6 and TPZ using hypoxia responsive HA-NI as a carrier. Owing to the low oxygen characteristics of cisplatin-resistant cells, T/C@HN NPs were specifically activated to achieve photodynamic therapy and programmed activation chemotherapy. This nanomedicine improved the specific recognition and inhibition efficiency of cisplatin resistant cells through synergistic therapy. It is encouraging to note that this nanomedicine has shown high efficacy in delaying tumor growth and reversing tumor resistance in PDX model therapy, and has great

potential in addressing treatment tolerance issues caused by hypoxia in tumor cells. This study provides a promising strategy for the treatment of lung tumors and a feasible basis for the treatment of drug-resistant tumors, thereby providing ideas for solving complex clinical problems.

CRedit authorship contribution statement

Yurong Liu: Writing – original draft, Visualization, Investigation, Formal analysis, Data curation. **Longqing Si:** Validation, Formal analysis, Data curation. **Yunheng Liu:** Validation, Formal analysis, Data curation. **Song Li:** Validation, Formal analysis, Data curation. **Xiaokang Zhang:** Validation, Formal analysis, Data curation. **Shaojing Jiang:** Validation, Formal analysis, Data curation. **Wenjing Liu:** Validation, Formal analysis, Data curation. **Xiaolin Li:** Validation, Formal analysis, Data curation. **Lianguo Zhang:** Validation, Formal analysis, Data curation. **Hongxia Zheng:** Validation, Formal analysis, Data curation. **Zhonghao Liu:** Project administration, Funding acquisition, Data curation. **Jinghui Hu:** Writing – review & editing, Project administration, Funding acquisition, Data curation, Conceptualization. **Jing Chen:** Writing – review & editing, Investigation, Funding acquisition, Formal analysis, Data curation, Conceptualization.

Declaration of competing interest

The authors declare that they have no known competing financial interests or personal relationships that could have appeared to influence the work reported in this paper.

Acknowledgements

This work was supported by the National Natural Science Foundation of China (No. 82102209), Natural Science Foundation of Shandong Province (No. ZR2022QE230), and Binzhou Medical College "Stomatology + X" University Integration Innovation Project (KQRH2024ZD003, KQRH2024MS002).

Appendix A. Supplementary data

Supplementary data to this article can be found online at <https://doi.org/10.1016/j.mtbio.2025.101709>.

Data availability

Data will be made available on request.

References

- Y.Y. Li, W.B. Lin, Platinum-based combination nanomedicines for cancer therapy, *Curr. Opin. Chem. Biol.* 74 (2023) 102290.
- A. Yamashita, et al., H-dot mediated nanotherapeutics mitigate systemic toxicity of platinum-based anticancer drugs, *Int. J. Mol. Sci.* 24 (20) (2023) 15466.
- B.Z. Yu, et al., Platinum prodrug nanoparticles with COX-2 inhibition amplify pyroptosis for enhanced chemotherapy and immune activation of pancreatic cancer, *Adv. Mater.* 36 (11) (2024) 2310456.
- S. Karakostas, et al., Global prevalence of cefiderocol non-susceptibility in Enterobacterales, *Pseudomonas aeruginosa*, *Acinetobacter baumannii*, and *Stenotrophomonas maltophilia*: a systematic review and meta-analysis, *Clin. Microbiol. Infection* 30 (2) (2024) 178–188.
- J. Yan, et al., Rewiring chaperone-mediated autophagy in cancer by a prion-like chemical inducer of proximity to counteract adaptive immune resistance, *Drug Resist. Updates* 73 (2024) 101037.
- M.J. Ko, et al., Magnetic nanoparticles for ferroptosis cancer therapy with diagnostic imaging, *Bioact. Mater.* 32 (2024) 66–97.
- M.S. Avila, et al., Carvedilol for prevention of chemotherapy-related cardiotoxicity, *J. Am. Coll. Cardiol.* 71 (20) (2018) 2281–2290.
- E.A. Dijkstra, et al., Locoregional failure during and after short-course radiotherapy followed by chemotherapy and surgery compared with long-course chemoradiotherapy and surgery, *Ann. Surg.* 278 (4) (2023) E766–E772.
- X. Guo, et al., Exosomal circular RNAs: a chief culprit in cancer chemotherapy resistance, *Drug Resist. Updates* 67 (2023) 100937.
- G.Q. Wei, et al., Recent progress in nanomedicine for enhanced cancer chemotherapy, *Theranostics* 11 (13) (2021) 6370–6392.

- [11] Y. Lu, et al., KYNU expression promotes cisplatin resistance in esophageal cancer, *J. Cancer* 15 (9) (2024) 2475–2485.
- [12] P. Qods, J. Arkat, Y. Batmani, Optimal administration strategy in chemotherapy regimens using multi-drug cell-cycle specific tumor growth models, *Biomed. Signal Process Control* 86 (3) (2023) 105221.
- [13] M.P. Rajan, C.K. Nanditha, A multi-drug pharmacokinetic optimal control approach in cancer chemotherapy, *J. Optim. Theor. Appl.* 195 (1) (2022) 314–333.
- [14] H.Y. Zhang, et al., Reversing multi-drug resistance by polymeric metformin to enhance antitumor efficacy of chemotherapy, *Int. J. Pharm.* 624 (2022) 121931.
- [15] L. Kelland, The resurgence of platinum-based cancer chemotherapy, *Nat. Rev. Cancer* 7 (8) (2007) 573–584.
- [16] L. Galluzzi, et al., Molecular mechanisms of cisplatin resistance, *Oncogene* 31 (15) (2012) 1869–1883.
- [17] L.N. Yan, et al., Nanoparticle-based drug delivery system: a patient-friendly chemotherapy for oncology, *Dose Response* 18 (3) (2020), 1559325820936161.
- [18] W. Yang, et al., Toxic epidermal necrolysis associated with chemoimmunotherapy for lymphoma: case report and literature review, *Immunotherapy* 14 (5) (2022) 275–282.
- [19] D.S. Wei, et al., Nuclear-targeting lipid Pt IV prodrug amphiphile cooperates with siRNA for enhanced cancer immunotherapy by amplifying Pt-DNA adducts and reducing phosphatidylserine exposure, *J. Am. Chem. Soc.* 146 (1) (2023) 1185–1195.
- [20] Z.Y. Gong, et al., Tumor acidic microenvironment-induced drug release of RGD peptide nanoparticles for cellular uptake and cancer therapy, *Colloids Surf. B Biointerfaces* 202 (2021) 111673.
- [21] J. Park, et al., Alliance with EPR effect: combined strategies to improve the EPR effect in the tumor microenvironment, *Theranostics* 9 (26) (2019) 8073–8090.
- [22] M.H. Cui, et al., Bioorthogonal guided activation of cGAS-STING by AIE photosensitizer nanoparticles for targeted tumor therapy and imaging, *Adv. Mater.* 35 (52) (2023) 2305668.
- [23] Z.X. Guan, et al., A specific targeted enhanced nanotherapy strategy for inducing ferroptosis by regulating the iron pool levels in tumor cells, *ACS Appl. Mater. Interfaces* 16 (42) (2024) 56837–56849.
- [24] T.T. Lang, et al., Prodrug-based nano-delivery strategy to improve the antitumor ability of carboplatin in vivo and in vitro, *Drug Deliv.* 28 (1) (2021) 1272–1280.
- [25] Y. Liang, et al., A NAG-guided nano-delivery system for redox- and pH-triggered intracellularly sequential drug release in cancer cells, *Int. J. Nanomed.* 15 (3) (2020) 841–855.
- [26] B.X. Ren, et al., Alteronol enhances the anti-tumor activity and reduces the toxicity of high-dose adriamycin in breast cancer, *Front. Pharmacol.* 10 (2019) 285.
- [27] L.Q. Wang, et al., An acquired vulnerability of drug-resistant melanoma with therapeutic potential, *Cell* 173 (6) (2018) 1413–1425.
- [28] D.S. Li, et al., Morusin, a novel inhibitor of ACLY, induces mitochondrial apoptosis in hepatocellular carcinoma cells through ROS-mediated mitophagy, *Biomed. Pharmacother.* 180 (2024) 117510.
- [29] H.C. Zhang, et al., A novel mechanism of 6-methoxydihydroavicine in suppressing ovarian carcinoma by disrupting mitochondrial homeostasis and triggering ROS/MAPK mediated apoptosis, *Front. Pharmacol.* 14 (2023) 1093650.
- [30] G.L. Xiong, et al., Near-infrared-II light induced mild hyperthermia activate cisplatin-artemisinin nanoparticle for enhanced chemo/chemodynamic therapy and immunotherapy, *Small Methods* 6 (9) (2022) 2200379.
- [31] M.G.V. Heiden, L.C. Cantley, C.B. Thompson, Understanding the warburg effect: the metabolic requirements of cell proliferation, *Science* 324 (5930) (2009) 1029–1033.
- [32] P.P. Hsu, D.M. Sabatini, Cancer cell metabolism: warburg and beyond, *Cell* 134 (5) (2008) 703–707.
- [33] M.G. Vander Heiden, Targeting cancer metabolism: a therapeutic window opens, *Nat. Rev. Drug Discov.* 10 (9) (2011) 671–684.
- [34] X.J. Liang, et al., SIRT1 contributes in part to cisplatin resistance in cancer cells by altering mitochondrial metabolism, *Mol. Cancer Res.* 6 (9) (2008) 1499–1506.
- [35] Z.Q. Lin, et al., A natural compound-empowered podophyllotoxin prodrug nanoassembly magnifies efficacy-toxicity benefits in cancer chemotherapy, *Asian J. Pharm. Sci.* 19 (4) (2024) 100892.
- [36] Z.H. Ai, et al., Overcoming cisplatin resistance of ovarian cancer cells by targeting HIF-1-regulated cancer metabolism, *Cancer Lett.* 373 (1) (2016) 36–44.
- [37] Z.X. Guan, et al., Self-enhanced targeted nanomedicines based on iron starvation acclimation for tumor-specific therapy, *Chem. Eng. J.* 495 (2024) 153371.
- [38] B. Thienpont, et al., Tumour hypoxia causes DNA hyper-methylation by reducing TET activity, *Nature* 537 (7618) (2016) 6–9.
- [39] W.Z. Li, et al., The anti-tumor efficacy of 20(S)-protopanaxadiol, an active metabolite of ginseng, according to fasting on hepatocellular carcinoma, *J. Ginseng Res.* 46 (1) (2022) 167–174.
- [40] D.S. Wei, et al., Breaking the intracellular redox balance with diselenium nanoparticles for maximizing chemotherapy efficacy on patient-derived xenograft models, *ACS Nano* 14 (12) (2020) 16984–16996.
- [41] J. Chen, et al., Exploiting the acquired vulnerability of cisplatin-resistant tumors with a hypoxia-amplifying DNA repair-inhibiting (HYDRI) nanomedicine, *Sci. Adv.* 7 (13) (2021) eabc5267.
- [42] Y.R. Liu, et al., Versatile nanomaterials that interfere with ferroptosis in the tumor microenvironment, *Int. J. Nanomed.* 20 (2025) 2461–2473.
- [43] G.B. Yang, et al., A hypoxia-responsive albumin-based nanosystem for deep tumor penetration and excellent therapeutic efficacy, *Adv. Mater.* 31 (25) (2019) e1901513.
- [44] P. Zhu, et al., MnOOH-catalyzed autoxidation of glutathione for reactive oxygen species production and nanocatalytic tumor innate immunotherapy, *J. Am. Chem. Soc.* 145 (10) (2023) 5803–5815.
- [45] C.Y. Wang, et al., Efficient piezocatalytic H₂O₂ production of atomic-level thickness Bi₄Ti₃O₁₂ nanosheets with surface oxygen vacancy, *Chem. Eng. J.* 431 (2022) 133930.
- [46] W.W. Wang, et al., Boosting ferroptosis via abiplatin (iv) for treatment of platinum-resistant recurrent ovarian cancer, *Nano Today* 44 (2022) 101459.
- [47] Y.Y. Liu, et al., Modulating hypoxia via nanomaterials chemistry for efficient treatment of solid tumors, *Accounts Chem. Res.* 51 (10) (2018) 2502–2511.
- [48] C. Zhang, et al., Magnesium silicide nanoparticles as a deoxygenation agent for cancer starvation therapy, *Nat. Nanotechnol.* 12 (4) (2017) 378–386.
- [49] J. Tang, et al., Openwork@Dendritic mesoporous silica nanoparticles for lactate depletion and tumor microenvironment regulation, *Angew. Chem. Int. Ed.* 59 (49) (2020) 22054–22062.
- [50] S. Wang, et al., The effect of lengths of branched-chain fatty alcohols on the efficacy and safety of docetaxel-prodrug nanoassemblies, *Acta Pharm. Sin. B* 14 (3) (2024) 1400–1411.
- [51] J.Y. Zhang, et al., Hypoxia-triggered tumor specific glutamine inhibition for reversing cisplatin resistance of chemotherapy, *Chem. Eng. J.* 479 (2024) 147692.
- [52] J. Chen, et al., Light-triggered retention and cascaded therapy of albumin-based theranostic nanomedicines to alleviate tumor adaptive treatment tolerance, *Adv. Funct. Mater.* 28 (17) (2018) 1707291.
- [53] J. Rutz, et al., Allyl-, butyl- and phenylethyl-isothiocyanate modulate Akt-mTOR and cyclin-CDK signaling in gemcitabine- and cisplatin-resistant bladder cancer cell lines, *Int. J. Mol. Sci.* 23 (19) (2022) 10996.
- [54] J.K. Salem, I.M. El-Nahhal, S.F. Salama, Determination of the critical micelle concentration by absorbance and fluorescence techniques using fluorescein probe, *Chem. Phys. Lett.* 730 (2019) 445–450.
- [55] Y. Shi, H.Q. Luo, N.B. Li, Determination of the critical micelle concentration, first critical micelle concentration and second critical micelle concentration of surfactants by resonance Rayleigh scattering method without any probe, *Spectrochim. Acta Mol. Biomol. Spectrosc.* 78 (5) (2011) 1403–1407.
- [56] C.R. Bartman, et al., Metabolic pathway analysis using stable isotopes in patients with cancer, *Nat. Rev. Cancer* 23 (12) (2023) 863–878.
- [57] Z.Y. Yao, J.H. Wu, Y. Fang, Moderate constraint facilitates association and force-dependent dissociation of HA-CD44 complex, *Int. J. Mol. Sci.* 24 (3) (2023) 2243.
- [58] P. Yi, et al., Overexpressed CD44 is associated with B-cell activation via the HA-CD44-AIM2 pathway in lupus B cells, *Clin. Immunol.* 255 (2023) 109710.